IEEE Photonics Journal
An IEEE Photonics Society Publication

Open Access

Fast Long-Range Photon Counting Depth Imaging With Sparse Single-Photon Data

Volume 10, Number 3, June 2018

Yan Kang
Lifei Li
Dawei Liu
Dongjian Li
Tongyi Zhang
Wei Zhao

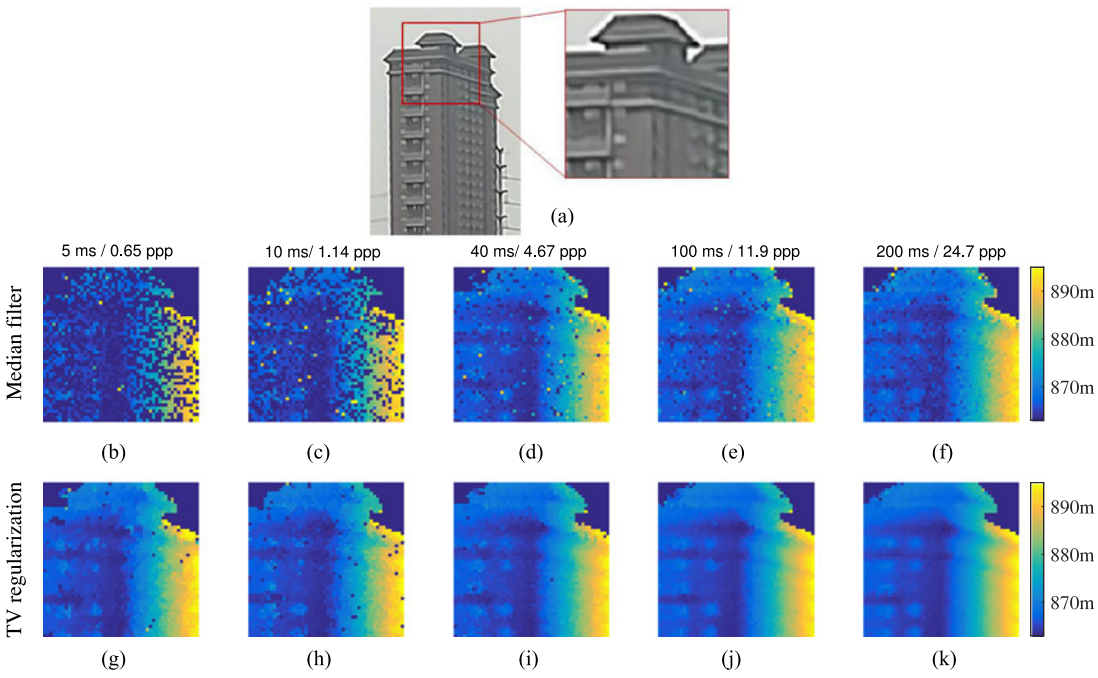

DOI: 10.1109/JPHOT.2018.2840681
1943-0655 © 2018 IEEE

IEEE photonics SOCIETY

IEEE

Fast Long-Range Photon Counting Depth Imaging With Sparse Single-Photon Data

Yan Kang,[1,2] **Lifei Li**,[1] **Dawei Liu**,[1,2] **Dongjian Li**,[1]
Tongyi Zhang,[1,2] **and Wei Zhao**[1,2]

[1]State Key Laboratory of Transient Optics and Photonics, Xi'an Institute of Optics and Precision Mechanics, Chinese Academy of Sciences, Xi'an 710119, China
[2]University of Chinese Academy of Sciences, Beijing 100049, China

DOI:10.1109/JPHOT.2018.2840681

Manuscript received May 13, 2018; accepted May 22, 2018. Date of publication May 25, 2018; date of current version June 15, 2018. This work was supported in part by the National Natural Science Foundation of China under Grant 61475191, in part by the Natural Science Basic Research Plan in Shaanxi Province of China under Grant 2017ZDJC-27, in part by the China North Industries Group Corporation (CNGC) "Process and technology" program under Grant KH2016003, and in part by the Chinese Academy of Sciences "Light of West China" Program under Grant XAB2015B24. Corresponding author: Tongyi Zhang (e-mail: tyzhang@opt.ac.cn).

Abstract: Fast depth imaging of noncooperative targets at a range of up to 900 m is demonstrated based on the time-of-flight time-correlated single-photon counting technique. Experimental results shown that our image system has the ability of reconstructing depth images with data of less than one photon per pixel. Especially, utilizing a modified total variation regularization algorithm with an optimal initial value, the acquisition time necessary for each pixel could be reduced by a factor of 8 compared to the traditional median filter approach, and the image processing time is extremely improved. This depth imaging system is a low-light-level device for a variety of applications, such as target detection, space surveillance, and distance measurement.

Index Terms: Photon counting, lidar, three-dimensional image acquisition, three-dimensional image processing.

1. Introduction

Single-photon counting lidar has attracted amount of attentions for long-range three-dimensional (3D) imaging for a number of remote sensing applications in recent years [1]–[9]. One of reasons is that the key component: Geiger mode avalanche photon diode detector (GmAPD) is already well developed, which has a substantial advantage of single-photon sensitivity and picosecond time resolution. When the avalanche photon diode's reverse-bias is above the breakdown voltage, it operates in a Geiger mode, in which the primary electron generated by the absorption of a single photon initiates a self-sustaining avalanche process. The avalanche process constitutes an electrical current surge with a sharp leading edge, which allows high-resolution timing [10]. The technology has found applications in airborne 3D imaging lidar, especially for terrain mapping and environmental monitoring [10]. The size, weight and power (SWaP) limitations imposed by air platforms demand a combination of high-sensitivity, low laser power, eye-safety and low cost [10]. Single-photon counting lidar is a candidate technology that potentially offers these advantages over more conventional analog lidars [10], [11]. Additional advantages of single-photon counting lidar also include high depth resolution and accuracy [12] which is improved by the time-correlated

single-photon counting (TCSPC) technique. TCSPC is a statistical sampling technique with picoseconds timing resolution based on the repetitive, precisely timed registration of single photons [12]–[15]. Due to these two techniques, single-photon counting lidar allows weaker laser sources to be used and time-of-flight data could be acquired from significantly longer ranges [16], [17], which can reduce SWaP index of the lidar systems as we desired.

In previous research of single photon counting 3D imaging, the acquisition time for one target must be long enough to detect hundreds of photons per pixel and even more data needs to be collected in the presence of background noise [18]–[21]. A reduction in the total acquisition time can be achieved by increasing the laser pulse energy or by increasing the repetition rate of the laser source. However, the high energy laser may cause the problem of eye-safety and high repetition may cause range aliasing problem. Although, random pattern techniques are suited for solving range aliasing problem [22], [23], it will increase complexity of hardware. In the alternative, effective signal processing algorithm could be an approach for improving the performance of single photon counting 3D imaging [5]–[7], [24]–[28]. In 2014, Kirmani *et al.* [5] reported the first-photon imaging technique, which exploits spatial correlations found in real-world scenes and the physics of low-flux measurements, can recover 3D structure and reflectivity from the first detected photon at each pixel. Then in 2016, using a 32×32 pixel silicon single-photon avalanche detector array combined with a computational imaging algorithm that exploits transverse smoothness and longitudinal sparsity of natural scenes, 3D imaging with a single photon per pixel is realized [7]. In very recently, a 10-km single photon counting depth imaging is implemented in reference [28] by using a normal total variation (TV) regularization method without initial value optimization, whereas the image processing time is relatively slow (i.e., 10 s), which needs be further improved.

In this paper, we demonstrated a fast long-range photon counting depth imaging system and the 3D image results of a 900-meter range non-cooperate target are obtained at sunset with less than one detected photon per pixel. Utilizing a modified TV regularization algorithm with optimal initial value, our image processing time is extremely reduced (i.e., 0.5 s), which is 20 times faster than reference [28]. And the acquisition time necessary for each pixel is also reduced by a factor of eight compared to traditional median filter approach.

2. Experiments

Up to now, there are many TCSPC 3D imaging systems developed by researchers. They can be divided into two categories, mono-static and bi-static. The advantages of the bi-static system include simple optical setup and no internal reflection interference. However, because of the fixed receiver optical system and the larger field of view for receiving, more background light comes to the receiving system. As to the mono-static system, the influence of background light is much less than that of bi-static, because only the background light from the illuminated area on the target can project into the detector. However, its disadvantages include more difficult adjustment of the optical path, and internal reflection coming from optical components which needs additional time gate subsystem to deal with. In this work, we adopt the simple bi-static mode incorporating with a GmAPD detector. The GmAPD used in our system is a single-element Si single-photon avalanche diode detector (SPCM-AQRH-16, Excelitas Technologies). According to the official specification of this GmAPD [29], the time resolution is $\sim$350 ps at its whole response spectrum (i.e., 400 nm–1060 nm). The depth imaging system used a microchip pulse laser (SNG-20F-100, Teem Photonics) operating at a wavelength of 532 nm, which generated 750 ps duration pulses at a repetition rate of 20 kHz.

The imaging system schematically illustrated in Fig. 1 was used to collect the photon arrival data and the system parameters were summarized in Table 1. The laser beam was collimated by two plano-convex lenses. The adjustable optical attenuator consisting of two polarization beam splitters and one half-wave plate (HWP) was used to control the laser output power. By rotating the HWP, minimum output power of 19 μW and maximum power of 28 mW were obtained (corresponding to pulse energy of 0.95 nJ and 1.4 μJ), respectively. The laser output was then reflected off a Thorlabs GVS012 two-axis galvo scanning system that raster scanned the beam over the target. The galvo

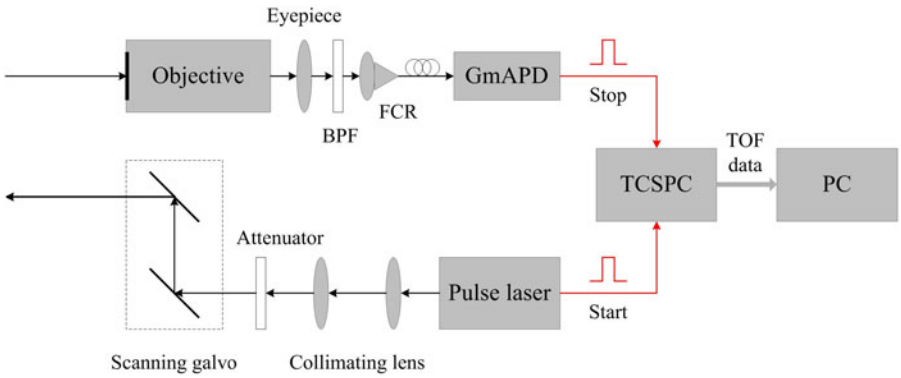

Fig. 1. Schematic diagram of the experimental setup of the imaging system operating in bi-static configuration with a scanned single-element GmAPD detector.

TABLE I

Summary of the Imaging System Parameters

System Parameter	Comment
Transmit and Receive	Bi-static: transmit and receive channels are separated
Laser	Microchip laser
Laser Repetition Rate	20 kHz
Illumination	532 nm
Laser Pulse Width	750 ps
Objective Lens	200 mm focal length, 78 mm diameter aperture
Average Output Power	19 μW $\sim$ 28 mW
Beam Scanning Mechanism	Galvanometer controlled mirrors
Spectral Filters	Bandpass: 1 nm Full Width at Half Maximum
Collection Fiber	62.5 μm diameter core, 1 meters long
Detector	Si GmAPD, 55% quantum efficiency at 532 nm
Instrument Response Function(jitter)	920 ps
Data Acquisition Hardware	PicoQuant HydraHarp 400

system took two analog voltage inputs (one for each axis, 0.5 V/degree) supplied by a Tektronix AFG 3252 function generator and the maximum mechanical scan angle was 20°. The objective lens collected the return photons from a target which were then subsequently collimated by an eyepiece. In order to suppress out-of-band background photons and reserve the signal photons, optic band pass filter (BPF) of 1 nm bandwidth was placed before the fiber coupling receiver (FCR) for the GmAPD detector. The photon detection events were time stamped relative to the laser pulse with high timing resolution using HydraHarp400 TCSPC module (PicoQuant, German). The device provided a count rate of up to 12.5 million counts/sec per channel and a 12 ps electrical timing resolution.

The characteristic of the complete TCSPC system that summarizes its overall timing precision is the Instrument Response Function (IRF) [30]. The overall IRF shape was a convolution of the laser pulse width, timing response of the electronics and the GmAPD detector jitter. As shown in Fig. 2, the IRF was obtained by directly scattering the detector with highly attenuated laser and binning the photon arrival times to generate a histogram of photon counts. Then a sum of three Gaussian base functions was fitted to the measured data by the Curve Fitting toolbox of MATLAB. Approximately 920 ps full width at half-maximum (FWHM) of IRF was measured over acquisition time of 60 s with a bin width of 1 ps. Theoretically, an estimate of the overall IRF width, assuming independent noise sources, can be obtained from the geometric sum of the individual components as an rms

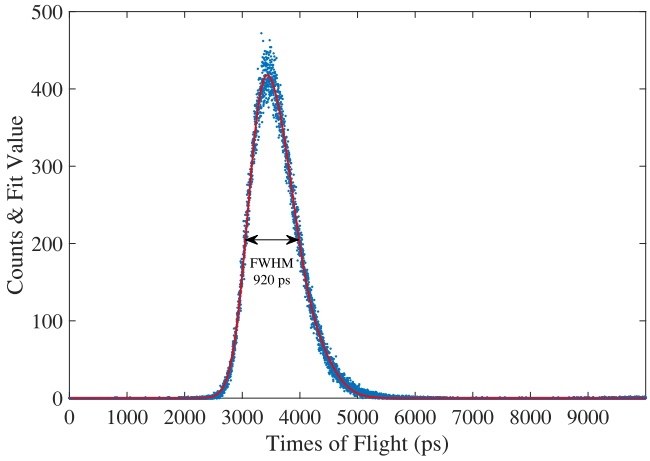

Fig. 2. Plot of the measured instrument response of the imaging system overlaid with fitted curve.

figure according to statistical error propagation laws [16]: $e_{system} = \sqrt{\sum e^2_{components}}$, which should be 828 ps. The reason for this inconformity may come from the millimetre-sized big laser spot, which may enlarge the width of IRF. During the experiments, the repetition rate of laser was not very stable for the mechanism of passively Q-Switched mode. Our experiments shown that, the laser repetition rate F_r fluctuated from 20.4 kHz to 20.9 kHz. Therefore, for the data acquisition part, the photon detection data was recorded under T2 mode of HydraHarp [31]. The return photons were divided into corresponding pixel position simply by the segmentation of total acquisition time.

3. Sparse Single-Photon Data Processing

To generate one complete data set, we raster scanned over $x_p \times y_p$ pixels with two-axis galvo system. Each pixel was illuminated with an equal acquisition time T_a seconds. Then the number of laser pulse emitted in one pixel is $N = T_a/T_r$. Here T_r is determined by the repetition rate F_r: $T_r = 1/F_r$. We recorded the total number of the observed photon detections $k_{i,j}$ along with their set of photon arrival times $T_{i,j} = \{t^{(1)}_{i,j}, t^{(2)}_{i,j}, \ldots, t^{(k_{i,j})}_{i,j}\}$ at each pixel. If $k_{i,j} = 0$, then $T_{i,j} = \varnothing$. Illuminating pixel (i, j) with pulse $s(t)$ results in back reflected light signal: $r_{i,j}(t) = x_{i,j}s(t - 2z_{i,j}/c) + b$, here $x_{i,j}$ denotes target reflectivity, $z_{i,j}$ denotes the object's 3D depth profile that we aim to recover, b denotes background light intensity, and c is the speed of light. The indices $i = 1, \ldots, x_p$ and $j = 1, \ldots, y_p$ represent the horizontal and vertical pixel coordinates, respectively. Then the rate function generating photon detections is derived as: $\lambda_{i,j}(t) = \eta r_{i,j} + d = \eta x_{i,j}s(t - 2z_{i,j}/c) + (\eta b + d)$, here η denotes the detection efficiency, d denotes detector's dark count rate. For notational convenience, the mean signal S and background count B per period are defined as $S = \int_0^{T_r} s(t)dt$ and $B = (\eta b + d)T_r$, respectively. Both S and B are assumed be known, because they can be measured before data acquisition.

Under the condition of low background and illuminating: $\eta x_{i,j}S + B \to 0$,the likelihood function $f_{T_{i,j}}$ of depth $z_{i,j}$ approximately satisfies [6], [32], [33]: $f_{T_{i,j}} \propto s(t - 2z_{i,j}/c)$. The log-likelihood function for estimation of depth from photon arrival times $t_{i,j}$ can be formed as: $L(z_{i,j}) = \sum_{\epsilon=1}^{k_{i,j}} log[s(t^{\epsilon}_{i,j} - 2z_{i,j}/c)]$. Natural scenes possess a typical scene structure–in depth as well as in reflectance–which is often described using sparsity in appropriate transform domains, such as discrete wavelet transform (DWT) or discrete cosine transform (DCT). Thus a regularization term is always added to describe the sparsity of the underlying image over the transform domain. In Ref. [5], [34], the l_1 norm based on DWT is applied to constrain the sparsity of image. In Ref. [33], [35], total variation semi-norm is selected as the regularization term. The use of TV in regularization can exploit image sparsity and

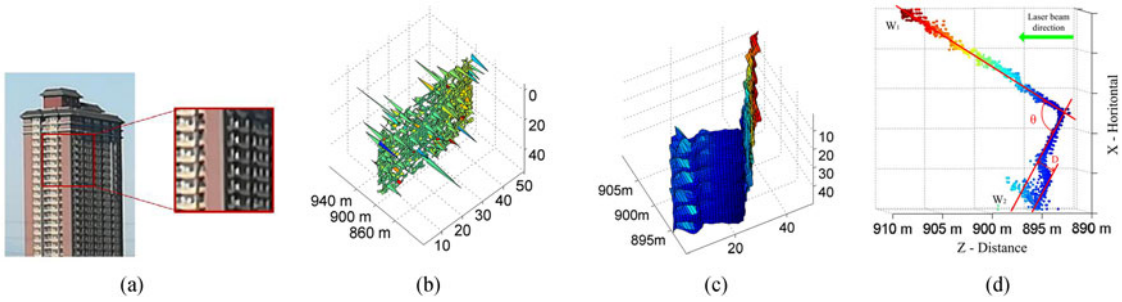

Fig. 3. (a) Photograph of a building's wall corner. (b) Median filtering result of depth image. (c) TV regularization result of depth image. (d) The top view of the depths plot of the target.

preserves edges [36]. Another advantage of TV regularization stems from the property that it can recover not only sparse signals or images, but also dense staircase signals or piecewise constant images. In other words, TV regularization would succeed when the gradient of the underlying signal or image is sparse [37]. Therefore, the total variation semi-norm $||z_{i,j}||_{TV}$ [38], a measure of the magnitude of all vertical and horizontal first-order differences, was used as the regularized term. The regularized ML estimate $\hat{z}_{i,j}$ for the depth image is thus obtained by solving the following convex optimization problem [5], [6]:

$$\hat{z}_{i,j} = argmin_z(1-\alpha)\sum_{i=1}^{xp}\sum_{j=1}^{yp} -L\left(z_{i,j}\right) + \alpha||z_{i,j}||_{TV} \qquad s.t.\ z_{i,j} \in (0, cT_r/2) \tag{1}$$

where α is a positive regularization parameter, choosing from $\{0.1, 0.2, \ldots, 0.9\}$ so that minimized the objective function defined in Eq. (1). The first term in the objective function corresponds to the likelihood term and the second term enforces transverse spatial structure across all the pixels.

Before solving the optimization problem for estimation of depth profile, two preparation work can be implemented to make the global optimum is found rapidly. The one is selecting an optimal value for empty pixels and the other is to censor the noise photon detection. We use rank-order mean (ROM) value $t_{i,j}^{(ROM)}$ [39], which is defined as the median value of all detection times at the 8 neighboring pixels of the current pixel, to replace each empty pixel, then these empty pixels can be initialized with an optimal value for that they borrow information from neighbor pixels. For censor noise photon detection, we use a simplified formula modified from reference [33], the set of uncensored signal photons is shown as:

$$U_{i,j} = \left\{\epsilon : |t_{i,j}^{(\epsilon)} - t_{i,j}^{(ROM)}| < \mu \cdot IRF_{width}, \epsilon = 1, \ldots, k_{i,j}\right\} \tag{2}$$

Thus $t_{i,j}^{(ROM)}$ and $U_{i,j}$ are used to initialize $t_{i,j}^{\epsilon}$ in Eq. (1) to enhance the solving speed. Here μ is an empirical factor, which is selected artificially as 4 in this experiments to get a better image result and this would be improved in future work.

Finally, the MATLAB toolbox SPIRAL-TAP [38], a Poisson reconstruction algorithm for constrained optimization problem, is used to solve the optimization problem with TV regularization term and it had been proved effective in reference [33]. For the reason that optimal initial value for empty pixels is choose, a loose nonmonotonic [38] parameters setting is used in SPIRAL, thus a relatively fast reconstruction speed can be realized in this experiments.

4. Results and Discussions

4.1 Depth Imaging of a 900-m Target of Residential Building

Fig. 3(a) shows a photograph of a building's wall corner taken with cell-phone camera. The depth image with 50 × 50 pixels was acquired with 10 ms acquisition time per pixel. Average over the

target, there was 2.5 photons detected per pixel, with 9.6% of the pixels having no detections. Fig. 3(b) shows depth imaging of the target with traditional median filter method. It can be seen that the shape of wall corner is covered by the noise and can't be identified. The result depth image of modified TV regularization method is shown in Fig. 3(c). In this depth image, we can not only identify the shape of the wall corner but also the projecting balcony on the left wall. A top view of the depths plot of the target is shown in Fig. 3(d) from which the right angle of the wall corner is easily observed.

In order to calculate the accurate value of the angle, we need to get the linear function of these two walls: W_1 and W_2. Here, we establish Cartesian coordinate based on the distance axis Z and horizontal axis X. A common form of a linear equation in the two variables Z and X is

$$X = mZ + H \tag{3}$$

where m determines the slope of the line and H determines the point at which the line crosses the X axis. A linear fit to the raw data points of the top view of W_1 and W_2 is given by $X = 0.498\ Z - 436.4$ and $X = -1.993Z + 1784.1$, respectively. Since

$$m = tan\beta \tag{4}$$

where β is the angle between the line and Z axis, then for $m_1 = 0.498$ and $m_2 = -1.993$, the abs slope of W_1 and W_2 is $\beta_1 = 26.47^\circ$ and $\beta_2 = 63.35^\circ$. Then the angle between the walls W_1 and W_2 can be calculated as $\theta = \beta_1 + \beta_2 = 89.82^\circ$, which is approximate to right angle. By calculating the distance between the data points of the wall and the balcony, we can obtained the depth D of balcony that is about 1.63 m.

4.2 Depth Imaging With Sparse Single-Photon Data

In order to validate the depth imaging quality and efficiency of the reconstruction algorithms under the circumstance of sparse single-photon data, the depth image with 50×50 pixels was acquired with different acquisition time per pixel (5 ms, 10 ms, 40 ms, 100 ms, 200 ms). Correspondingly, average over the target, there was 0.67, 1.14, 4.67, 11.9 and 24.7 photon detected per pixel (ppp), respectively. Fig. 4(a) shows photograph of the target building's roof taken with cell-phone camera. Depth images of the target were generated using traditional median filter approach seeing Fig. 4(b)–(f). These figures are compared to those obtained when using the modified TV regularization algorithm, as shown in Fig. 4(g)–(k).

Note that both algorithms were applied on single-photon data with an acquisition times per pixel varying from 5 ms to 200 ms. At the 200 ms acquisition time per pixel, the depth image reconstructed with the median filter and the modified TV regularization shown comparable image quality, i.e., the shape of the roof and some windows on the wall can be identified. For median filter approach, as the acquisition time decreases the identification of detail is significantly degrade, at 10 ms (1.14 ppp), only 63.6% of the pixels have generated a depth measurement and these pixels contain errors in depth, preventing target reconstructed and identification. Until the acquisition time reached 40 ms (4.67 ppp), the detail information of roof and window can be recognized. However, the modified TV regularization algorithm with optimal initial value can restore empty pixels in the data array well, such as the roof and some windows on the wall were recovered at 5 ms (0.65 ppp) acquisition time per pixel. So it can be thought that, the acquisition time necessary for each pixel is reduced by a factor of eight compared to median filter. These results also prove that the modified TV regularization algorithm has the ability of identification detail information and restoration of the missing pixels with sparse single-photon data less than 1 photon detected per pixel. However, the resulting depth images based on TV regularization method ignored some other details of the target (e.g., the white water pipes in the left side of target photograph and some windows in right side of target photograph shown in Fig. 4(a)). One of the potential reasons could been that TV regularization depends on a smoothness assumption, in general, TV semi-norm measures how much an image varies across pixels, so that a highly textured or noisy image will have a large TV semi-norm, while a smooth or

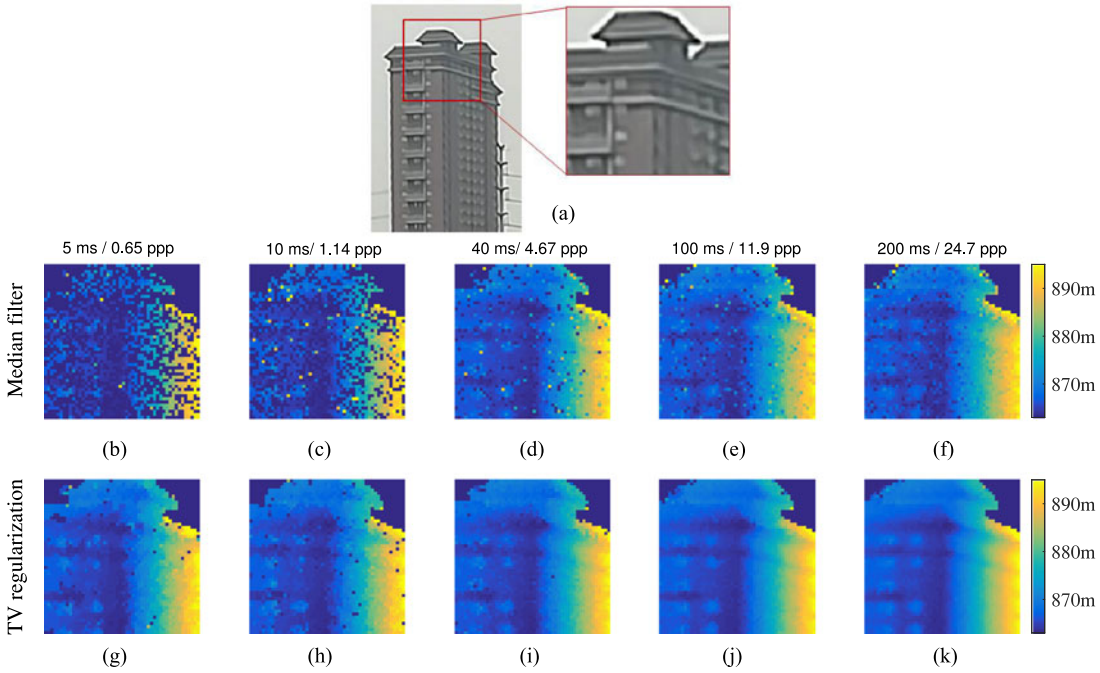

Fig. 4. (a) Photograph of a building's roof. (b)–(f) Median filtering results of depth image with different number of photons per pixel. (g)–(k) TV regularization results of depth image with different number of photons per pixel.

TABLE II

Achieved RSNR and Processing Time of Median Filter and TV Regularization

Acquisition time per pixel	PPP	Median filter		TV regularizaiton	
		RSNR	processing time	RSNR	processing time
200 ms	24.7	12.70 dB	0.0015 s	Infinity	0.4856 s
100 ms	11.9	12.52 dB	0.0014 s	14.63 dB	0.4951 s
40 ms	4.67	9.77 dB	0.0015 s	12.34 dB	0.4893 s
10 ms	1.14	4.54 dB	0.0015 s	11.90 dB	0.4976 s
5 ms	0.65	2.76 dB	0.0015 s	9.65 dB	0.5017 s

piecewise constant image would have a relatively small TV semi-norm. Therefore, the limitation of TV regularization is to assume spatial smoothness of the scene to mitigate the effect of noise.

To evaluate the performance of modified TV regularization and median filter methods quantitatively, reconstruction signal-to-noise ratio (RSNR) is calculated as Eq. (5) for depth image [28],

$$RSNR = 10\log_{10}\left(\frac{||z_{ij}^{\text{ref}}||^2}{||\hat{z}_{ij} - z_{ij}^{\text{ref}}||^2}\right) \tag{5}$$

where z_{ij}^{ref} is the reference depth image defined as the processed depth image for highest acquisition time, $\hat{z}_{ij}$ is the reconstructed depth image and $||\cdot||$ denotes the l_2 norm. Meanwhile the processing time of each image results using median filter and modified TV regularization methods is recorded. The computer using for run MATLAB code has a CPU of Intel(R)Core(TM) i7-2600 @3.40GHz and a 8G RAM. Loose nonmonotonic parameters are set as a tolerance of 1×10^{-5} and a maximum of 10 iterations.

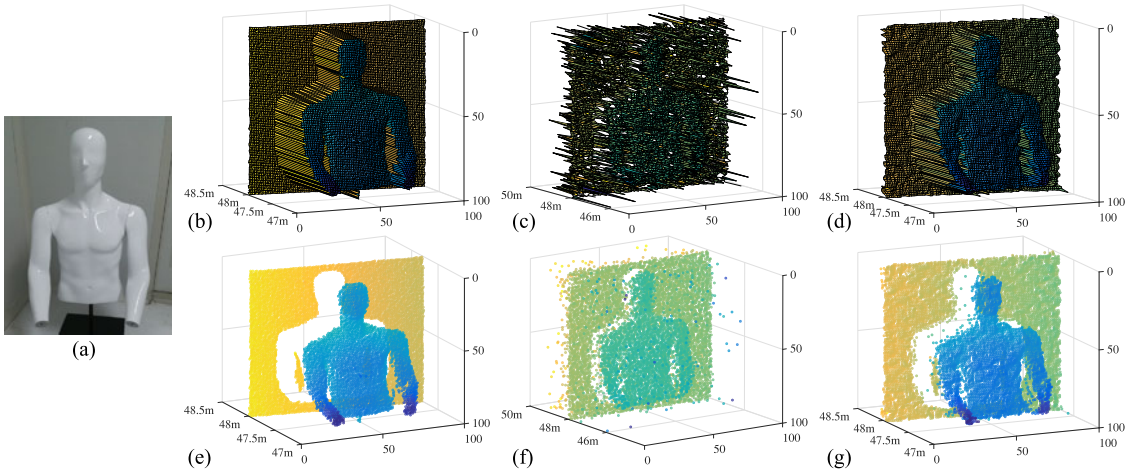

Fig. 5. (a) Photograph of a life-size mannequin. (b) and (e) Ground truth depth images. (c) and (f) Median filter results of depth image. (d) and (g) TV regularization results of depth image. (b)–(d) and (e)–(g) are displayed with 3D surf plot and 3D scatter plot MATLAB functions, relatively.

Finally, the result RSNR and processing times were obtained and shown in Table 2. We seen that the median filter was very fast for its small amount of computations. For modified TV regularization algorithm with optimal initial value, the number of empty pixels has no obvious effect on processing time. But, as to the normal TV regularization method (i.e., without optimal initial value), the processing time increases as the number of empty pixel increasing [28], because it needs more time to reconstruct the empty pixels. It is worth to mentioned that our image processing time is reduced to 0.5 s because of optimal initial value setting, which is 20 times faster than reference [28]. For the RSNR index, from the results presented in Table 2 and Fig. 4, we can see that the RSNR reduced as the acquisition time was shortened for both median filter and modified TV regularization approaches. The RSNR of modified TV regularization at 5 ms is as good as the RSNR of median filter method at 40 ms. It further quantitatively validates that the acquisition time necessary for each pixel could be reduced by a factor of eight by modified TV regularization approach. When the total time cost is considered, namely, the acquisition time and processing time are added up, the advantage of TV regularization is not obvious. However, when the long acquisition time is not allowed (e.g., energy of platform is limited or moving target detection), the number of photon return is very small (e.g., PPP is less than 1). In this case, performance of median filter (2.76 dB) is much worse than performance of TV regularization (9.65 dB), seeing Table 2 and Fig. 4. Therefore, TV regularization is suitable approach to reconstruct the depth image under photon-limited circumstance.

In order to further study the performance of imaging system and imaging algorithms, we select a cooperative target, the life-size mannequin (Fig. 5(a)), as the imaging target, which is about 48 meters distant from the imaging system. Ground truth depth image (Fig. 5(b) and (e)) could be reconstructed using a maximum likelihood method [24] at long acquisition time as 100 ms per pixel. The mean photon counts over all pixels was 335.5. The test dataset for Fig. 5(c), (d) and (f), (g) was obtained at short acquisition time as 1 ms per pixel with mean counts of 3.3 and miss pixels of 7.3%. To evaluate the image reconstruction quality, another factor of root mean square error (RMSE) value was calculated as Eq. (6) showing.

$$RMSE = \sqrt{\frac{1}{x_p y_p} \sum_{i=1}^{x_p} \sum_{j=1}^{y_p} \left(\hat{z}_{ij} - z_{ij}^{\text{ref}} \right)^2} \tag{6}$$

The experimental results were summarized as Fig. 5 and Table 3 showing. For the sake of observation and comparison, Fig. 5(b)–(d) and (e)–(g) were displayed with 3D surf plot and 3D scatter plot MATLAB functions, relatively. It could be seen that the median filtering results were contaminated by noise to some degree and there were some empty pixels in the depth image. On the contrary,

TABLE III
Achieved RMSE of Median Filter and TV Regularization

	Median filtering	TV regularization
RMSE	0.259 m	0.067 m

by utilizing TV regularization, the empty pixel was restored and the quality of depth image was improved. As shown from Table 3, the TV regularization method had a 74% decrease of RMSE on depth imaging.

Besides, the operating range of our depth imaging system can be analyzed by lidar range equation [3] shown as follow,

$$N_{sig} = \frac{E_T \lambda}{hc} \cdot \frac{\rho_t A_t}{A_{illum}} \cdot \frac{A_{rec}}{\pi R^2} \cdot \eta_{atm}^2 \cdot \eta_{sys} \cdot \eta_d \tag{7}$$

where N_{sig} is the return signal photon number per laser pulse. $E_T \lambda / hc$ is the emission photon number per laser pulse (h is the Planck's constant and c is the speed of light), proportional to the pulse energy E_T of the laser and the wavelength λ of laser. ρ_t denotes the target reflectance. A_{rec} denotes area of the receiver. η_{atm} denotes laser's transmission efficiency through the atmosphere, which can be expressed as a function of the target range R and the atmospheric attenuation factor μ_a (i.e., $\eta_{atm} = e^{-\mu_a R}$). η_{sys} denotes receiver optical system's efficiency and it is measured as 0.07 using the method in reference [40]. The value of η_{sys} is not very high for the reason of optical elements' attenuation (i.e., band pass filter, objective lens, eyepiece and fiber), fiber coupling losses and possible misalignment of the optical system. In future work, the receiver optical system's efficiency need be improved. η_d denotes the detector's single-photon detection efficiency, which is given as about 55% at 532 nm. Assuming that illuminating area A_{illum} and cross section area A_t are equal, and the reflectance of the target is 0.1, and the atmospheric attenuation factor is 0.17 km^{-1}. Our TCSPC lidar system is operated with photon rates of 10% (i.e., 0.1 photon return per laser pulse) or less in order to avoid range bias [41]. Therefore, with maximum pulse energy of 1.4 μJ, the maximum detection range of our system can be calculated as 5.6 km. According to Eq. (7), if we improve the receiver optical system's efficiency or the laser power or the area of the receiver, the maximum detection range of our depth imaging system will be further improved.

5. Conclusion

In summary, we have demonstrated a fast long-range photon counting depth imaging system based on a modified TV regularization algorithm with optimal initial value and the 3D images can be reconstructed with less than one detected photon per pixel. Compared with the previous photon counting 3D imaging system, the acquisition time and image processing time of our system are both extremely reduced, which promotes this technique in practical engineering applications. In future, a more eye-safety laser wavelength will be choose as the illumination source, and the experiments will be carried out in varying weather conditions and different times of the day.

References

[1] A. Mccarthy, R. J. Collins, N. J. Krichel, V. Fernandez, A. M. Wallace, and G. S. Buller, "Long-range time-of-flight scanning sensor based on high-speed time-correlated single-photon counting," *Appl. Opt.*, vol. 48, no. 32, pp. 6241–6251, 2009.
[2] M. S. Oh, H. J. Kong, T. H. Kim, S. E. Jo, B. W. Kim, and D. J. Park, "Development and analysis of a photon-counting three-dimensional imaging laser detection and ranging (LADAR) system," *J. Opt. Soc. Amer. A, Opt. Image Sci. Vision*, vol. 28, no. 5, pp. 759–765, 2011.
[3] P. F. McManamon, "Review of ladar: A historic, yet emerging, sensor technology with rich phenomenology," *Opt. Eng.*, vol. 51, no. 6, 2012, Art. no. 060901.
[4] W. He, B. Sima, Y. Chen, H. Dai, Q. Chen, and G. Gu, "A correction method for range walk error in photon counting 3d imaging lidar," *Opt. Commun.*, vol. 308, pp. 211–217, 2013.

[5] A. Kirmani *et al.*, "First-photon imaging," *Science*, vol. 343, no. 6166, pp. 58–61, 2014.
[6] D. Shin, A. Kirmani, V. K. Goyal, and J. H. Shapiro, "Photon-efficient computational 3-D and reflectivity imaging with single-photon detectors," *IEEE Trans. Comput. Imag.*, vol. 1, no. 2, pp. 112–125, Jun. 2015.
[7] D. Shin *et al.*, "Photon-efficient imaging with a single-photon camera," *Nature Commun.*, vol. 7, 2016, Art. no. 12046.
[8] W. He *et al.*, "Adaptive depth imaging with single-photon detectors," *IEEE Photon. J.*, vol. 9, no. 2, Apr. 2017, Art. no. 7801812.
[9] V. Molebny, P. McManamon, O. Steinvall, T. Kobayashi, and W. Chen, "Laser radar: Historical prospective—From the East to the West," *Opt. Eng.*, vol. 56, no. 3, 2017, Art. no. 031220.
[10] M. E. O'Brien and D. G. Fouche, "Geiger-mode avalanche photodiodes for three-dimensional imaging," *Lincoln Lab. J.*, vol. 13, no. 2, pp. 335–350, 2002.
[11] R. A. Lamb, "A technology review of time-of-flight photon counting for advanced remote sensing," *Proc. SPIE*, vol. 768, 2010, Art. no. 768107.
[12] P. A. Hiskett and R. A. Lamb, "Design considerations for high-altitude altimetry and lidar systems incorporating single-photon avalanche diode detectors," *Proc. SPIE*, vol. 8033, 2011, Art. no. 80330F.
[13] G. Buller and A. Wallace, "Ranging and three-dimensional imaging using time-correlated single-photon counting and point-by-point acquisition," *IEEE J. Sel. Topics Quantum Electron.*, vol. 13, no. 4, pp. 1006–1015, Jul./Aug. 2007.
[14] J. S. Massa, G. S. Buller, A. C. Walker, S. Cova, M. Umasuthan, and A. M. Wallace, "Time-of-flight optical ranging system based on time-correlated single-photon counting," *Appl. Opt.*, vol. 37, no. 31, 1998, Art. no. 7298.
[15] W. Becker, *Advanced Time-Correlated Single Photon Counting Techniques*. Berlin, Germany: Springer, 2005, pp. 104–112.
[16] D. V. O'Connor and D. Phillips, *Time-Correlated Single Photon Counting*. San Francisco, CA, USA: Academic, 1984, pp. 157–168.
[17] P. A. Hiskett, K. J. Gordon, and R. A. Lamb, "Advanced 3D imaging lidar concepts for long range sensing," *Proc.SPIE*, vol. 9114, 2014, Art. no. 91140G.
[18] P. A. Hiskett, G. S. Buller, R. A. Lamb, A. M. Pawlikowska, R. M. Pilkington, and K. J. Gordon, "Long-range 3D single-photon imaging lidar system," *Proc.SPIE*, vol. 9250, 2014, Art. no. 925007.
[19] M. A. Diagne *et al.*, "Integrated array of 2-μm antimonide-based single-photon counting devices," *Opt. Exp.*, vol. 19, no. 5, pp. 4210–4216, 2011.
[20] A. Mccarthy *et al.*, "Kilometer-range, high resolution depth imaging via 1560 nm wavelength single-photon detection," *Opt. Exp.*, vol. 21, no. 7, pp. 8904–8015, 2013.
[21] Z. Zhang, Y. Xu, L. Wu, Y. Zhang, Y. Zhao, and J. Su, "Photon counting range-intensity image strategy in low-light level environments," *Opt. Lett.*, vol. 39, no. 8, pp. 2467–2470, 2014.
[22] P. A. Hiskett, C. S. Parry, A. Mccarthy, and G. S. Buller, "A photon-counting time-of-flight ranging technique developed for the avoidance of range ambiguity at gigahertz clock rates," *Opt. Exp.*, vol. 16, no. 18, pp. 13685–13698, 2008.
[23] N. J. Krichel, A. Mccarthy, and G. S. Buller, "Resolving range ambiguity in a photon counting depth imager operating at kilometer distances," *Opt. Exp.*, vol. 18, no. 9, pp. 9192–9206, 2010.
[24] D. Shin, J. H. Shapiro, and V. K. Goyal, "Single-photon depth imaging using a union-of-subspaces model," *IEEE Signal Process. Lett.*, vol. 22, no. 12, pp. 2254–2258, Dec. 2015.
[25] Y. Altmann, X. Ren, A. Mccarthy, G. S. Buller, and S. Mclaughlin, "Lidar waveform-based analysis of depth images constructed using sparse single-photon data," *IEEE Trans. Image Process.*, vol. 25, no. 5, pp. 1935–1946, May 2016.
[26] A. Halimi *et al.*, "Restoration of intensity and depth images constructed using sparse single-photon data," in *Proc. Signal Process. Conf.*, 2016, pp. 86–90.
[27] Y. Kang, L. Li, X. Duan, T. Zhang, D. Li, and W. Zhao, "Photon-limited depth and reflectivity imaging with sparsity regularization," *Opt. Commun.*, vol. 392, no. 1, pp. 25–30, 2017.
[28] A. M. Pawlikowska, A. Halimi, R. A. Lamb, and G. S. Buller, "Single-photon three-dimensional imaging at up to 10 kilometers range," *Opt. Exp.*, vol. 25, no. 10, pp. 11919–11931, 2017.
[29] 2018. [Online]. Available: www.excelitas.com/Downloads/DTS_SPCM-AQRH.pdf
[30] M. E. O'Brien and D. G. Fouche, "Simulation of 3D laser radar systems," *Lincoln Lab. J.*, vol. 15, no. 1, pp. 37–60, 2005.
[31] 2018. [Online]. Available: www.picoquant.com/images/uploads/downloads/hydraharp400.pdf
[32] D. Shin, "Computational 3D and reflectivity imaging with high photon efficiency," Master's thesis, Massachusetts Inst. Technol., Cambridge, MA, USA, 2014.
[33] D. Shin, A. Kirmani, V. K. Goyal, and J. H. Shapiro, "Computational 3D and reflectivity imaging with high photon efficiency," in *Proc. IEEE Int. Conf. Image Process.*, 2015, pp. 46–50.
[34] A. Kirmani, D. Venkatraman, A. Colaço, F. N. C. Wong, and V. K. Goyal, "High photon efficiency computational range imaging using spatio-temporal statistical regularization," in *Proc. Conf. Lasers Electro-Opt.*, 2013, pp. 1–2.
[35] A. Kirmani, A. Colaço, D. Shin, and V. K. Goyal, "Spatio-temporal regularization for range imaging with high photon efficiency," *Proc.SPIE*, vol. 8858, 2013, Art. no. 88581F.
[36] J. Yang, Y. Zhang, and W. Yin, "A fast alternating direction method for TVL1-l2 signal reconstruction from partial fourier data," *IEEE J. Sel. Topics Signal Process.*, vol. 4, no. 2, pp. 288–297, Apr. 2010.
[37] C. Li, "An efficient algorithm for total variation regularization with applications to the single pixel camera and compressive sensing," Master's thesis, Rice Univ., Houston, TX, USA, 2009.
[38] Z. T. Harmany, R. F. Marcia, and R. M. Willett, "This is spiral-tap: Sparse Poisson intensity reconstruction algorithms—Theory and practice," *IEEE Trans. Image Process.*, vol. 21, no. 3, pp. 1084–1096, Mar. 2012.
[39] E. Abreu, M. Lightstone, S. K. Mitra, and K. Arakawa, "A new efficient approach for the removal of impulse noise from highly corrupted images," *IEEE Trans. Image Process.*, vol. 5, no. 6, pp. 1012–1025, Jun. 1996.
[40] N. J. Krichel *et al.*, "Long-range depth profiling based on time-correlated single-photon counting," Ph.D. dissertation, Heriot-Watt Univ., Edinburgh, U.K., 2011.
[41] C. B. Clarke and J. J. Degnan, "Processing single photon data for maximum range accuracy," in *Proc. Int. Workshop Laser Ranging*, 2013, p. 13-0413.